ELSEVIER

Synthesis and characterization of mixed-morphology CePO$_4$ nanoparticles

L. Karpowich[a], S. Wilcke[b], Rong Yu[c], G. Harley[a], J.A. Reimer[b], L.C. De Jonghe[a,c,*]

[a]*Department of Materials Science and Engineering, University of California at Berkeley, Berkeley, CA 94720, USA*
[b]*Department of Chemical Engineering, University of California at Berkeley, Berkeley, CA 94720, USA*
[c]*Materials Sciences Division, Lawrence Berkeley National Laboratory, Berkeley, CA 94720, USA*

Abstract

Cerium phosphate nanoparticles with diameters of 10–180 nm were synthesized by a variety of solution techniques. X-ray diffraction (XRD) determined the crystalline phase(s) present in each sample. Population, shift, and spin-lattice relaxation ^{31}P solid-state nuclear magnetic resonance (NMR) measurements accounted for all the ^{31}P nuclei expected in each sample, and were able to distinguish between phosphorous nuclei in different environments and phases. Transmission electron microscopy (TEM) characterized the morphology and crystallinity of the powder samples as well as of the sintered compacts of the powders. In conjunction with TEM, energy-dispersive spectroscopy (EDS) provided a measure of the composition of the bulk intergranular regions within each CePO$_4$ sample. The presence of an amorphous, phosphate-rich intergranular phase was found in those samples prepared by dissolution of ceria in H$_3$PO$_4$ under various conditions.

© 2006 Elsevier Inc. All rights reserved.

Keywords: CePO$_4$; Cerium phosphate; Monazite; Nanoparticle; ^{31}P solid-state NMR

1. Introduction

Cerium orthophosphate is a synthetic analog of the naturally occurring mineral monazite, which often contains trace amounts of La, Th, and other rare-earth elements [1,2] and possesses the most stable chemical properties of naturally occurring minerals [3]. Monazite cerium phosphate is also a heat-stable phosphate with a melting temperature close to 2000 °C [2], making CePO$_4$ attractive for use in high-temperature, ceramic applications. Cerium phosphate has been studied as a potential storage material for nuclear waste [4], a poison to automobile catalyst [5,9] and, more recently, as a potential proton conduction membrane for use in hydrogen fuel cells [10]. Studies have shown that the chemical nature and particle size of synthesized phosphates is highly dependent on the processing technique [11–15]. To clarify the relationship between the synthetic route and the chemical nature, CePO$_4$ was synthesized by different methods and examined by X-ray Diffraction (XRD), transmission electron microscopy (TEM), energy-dispersive spectroscopy (EDS), and ^{31}P solid-state nuclear magnetic resonance (NMR).

2. Experimental methods

Four different samples of CePO$_4$, both commercially purchased and in-house synthesized, were studied. Sample 1 was 99% pure cerium (III) phosphate powder in the rhabdophane phase, as purchased from Alfa Aesar (AA39215-22). Sample 2 was prepared by heating the as-received powder at 800 °C in air for 8 h, resulting in a transformation to the monazite phase. Samples 3 and 4 were synthesized via reaction between CeO$_2$ powder (Nanostructured & Amorphous Materials, Inc., 99.95%) and liquid H$_3$PO$_4$ (J.T. Baker Analyzed ACS Reagent, 85%). Cerium oxide and phosphoric acid were combined in acetone with a ratio of P:Ce = 1:1, and the suspensions were attritor milled for 2 h at 400 RPM. After drying overnight, the resulting powders were ground in an alumina
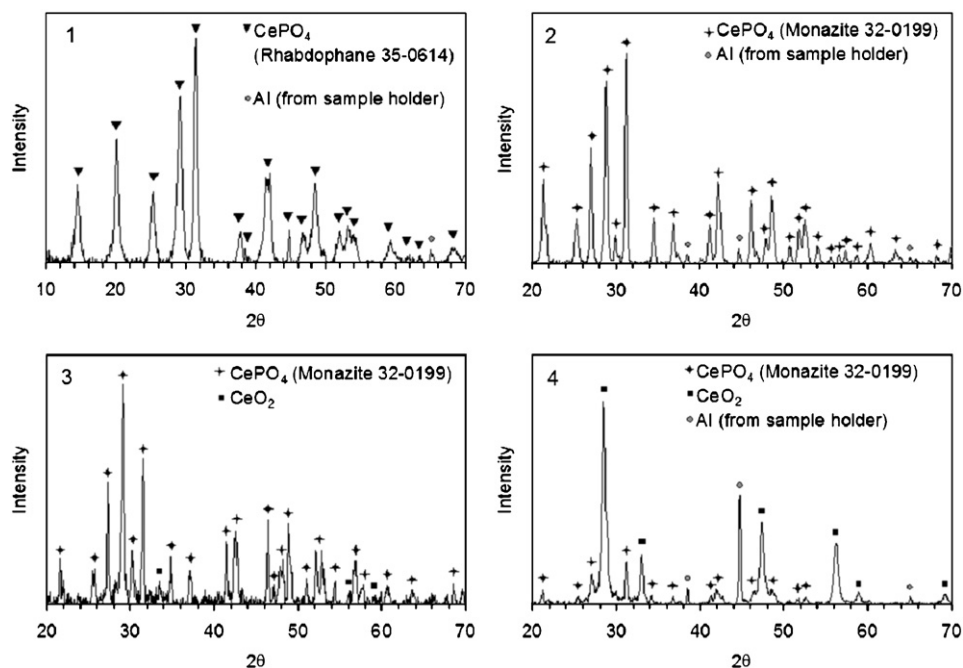
Fig. 1. X-ray diffraction (XRD) measurements of rhabdophane $CePO_4$ (Sample 1), monazite $CePO_4$ (Sample 2), and mixtures of $CePO_4$ and CeO_2 (Samples 3 and 4).
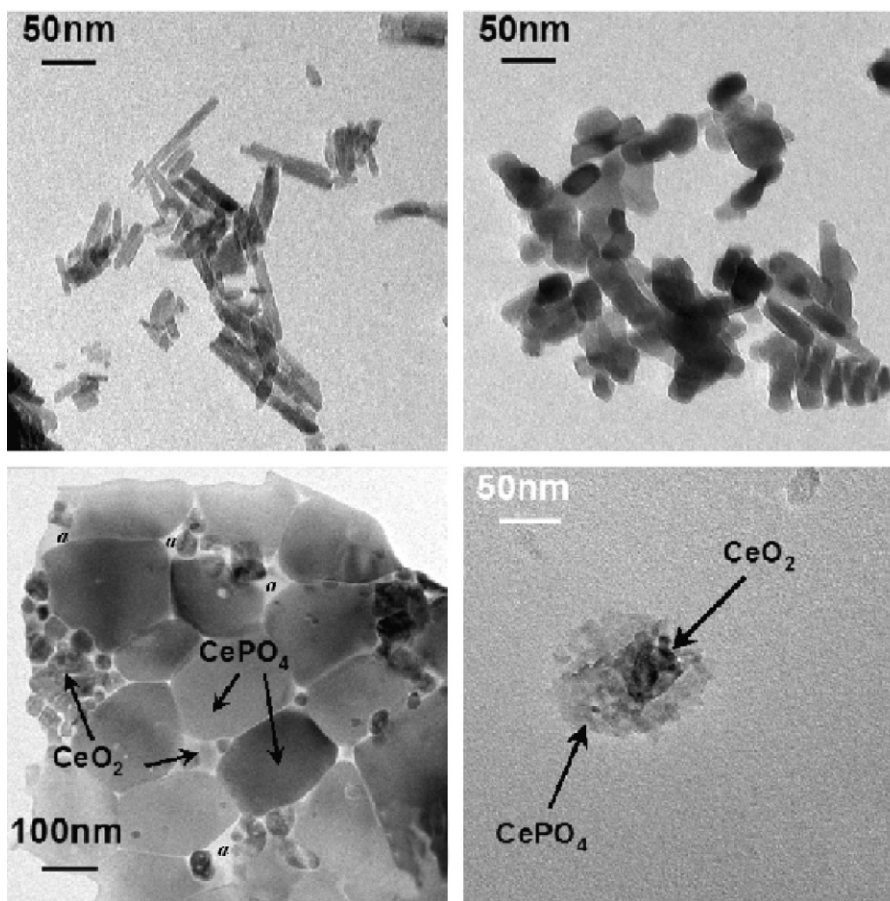

Fig. 2. Transmission electron microscopy (TEM) images showing the morphology of Samples 1–4. Sample 1: TEM image of shows a needle-shaped rhabdophane crystallite supported on an amorphous carbon film. Sample 2: After 8 h at 800 °C, the as-received powder has transformed into equiaxed monazite powder. Sample 3: the larger particles are monazite $CePO_4$, while the smaller particles are unreacted CeO_2. Amorphous material is also present between the grains (marked as *a*) Sample 4: powder composite particle after reaction of a ceria powder with phosphoric acid at 100 °C. The darker core particle ($\sim$50 nm) is unreacted or partly reacted CeO_2, while the lighter, outer particles ($\sim$10–20 nm) are monazite ($CePO_4$) that accumulated around the ceria particle either as a result of the reaction topology or as a result of hetero-agglomeration.
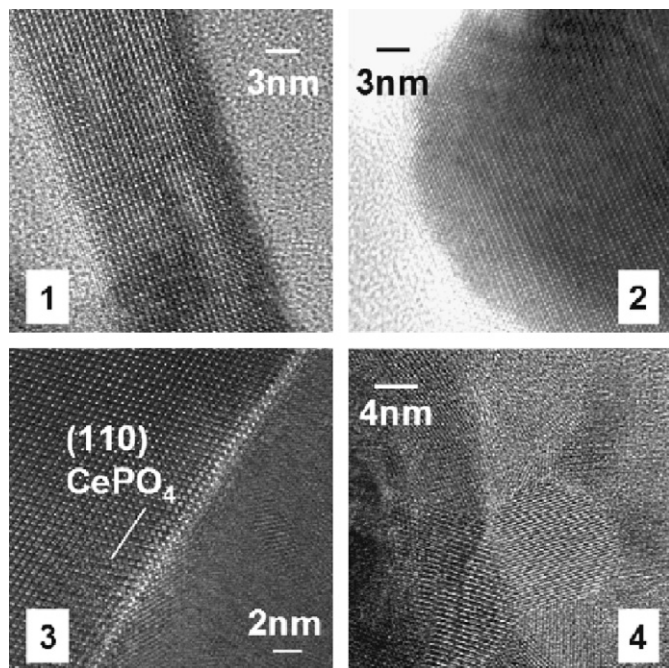
Fig. 3. Transmission electron microscopy (TEM) lattice images of CePO$_4$ particles in Samples 1–4. Sample 1: crystalline rhabdophane needle on amorphous support film. Sample 2: monazite particle; no amorphous phosphate phase is present. Sample 3: crystalline monazite; in addition, TEM also found amorphous phosphate in between grains (see also Fig. 2-Sample 3). Sample 3: the (1 1 0) CePO$_4$ plane is indicated in the high resolution TEM image of a crystalline monazite. Sample 4: TEM close-up of the small, crystalline monazite particles surrounding the central ceria particle shown in Fig. 2-Sample 4.

mortar and pestle and sieved with US Standard #325 stainless steel sieve. Sample 3 powder was then uniaxially die-pressed at 3000 psi followed by a cold isostatic press at 180 kpsi. The resulting pellets were calcined and free-sintered at 800 °C for 20 h. Sample 4 was similarly synthesized by placing CeO$_2$ and H$_3$PO$_4$ (P:Ce = 1:1) in acetone, attritor milling, then heating to 100 °C for 2 h with magnetic stirring, and drying overnight under ambient pressure and temperature. The powder was then ground, and sieved as described above.

The four resulting powders, as well as Sample 3 pellets, were characterized with XRD to identify the crystalline phases present. A Siemens D500 diffractometer and Phillips Analytical X'Pert PRO MP diffractometer were used with CuKα radiation, and step size of 0.05°2θ from 10° to 70°. Patterns were matched using the international center for diffraction data (ICDD)–powder diffraction files (PDF) database.

Powder samples 1, 2, and 4 were prepared for TEM analysis by dropping dilute specimen suspensions on copper grids covered with amorphous carbon films. TEM foils were prepared from Sample 3, first grinding slices down to 80 μm and mechanically dimpling these to 10 μm, followed by ion milling to electron transparency. The TEM experiments were carried out using a Philips CM200 microscope, operating at 200 kV. The point resolution of

this microscope is 0.23 nm and the information limit is 0.16 nm. Chemical composition analysis was done by EDS.

^{31}P NMR spectra were acquired at 1.54 T in a Doty probe tuned to a frequency of 26.56 MHz using a home-built spectrometer with a Tecmag console. Shift and population measurements were referenced to aqueous 85% H$_3$PO$_4$ (Fisher-Scientific). A 1.7 μs 90° single pulses was used for the shift, peak width, and population measurements of each sample. An inversion recovery experiment determined the spin-lattice relaxation time, T_1, while a Hahn echo with varying τ delays measured the spin–spin relaxation time, T_2. All shift, peak width, T_1 and T_2 measurements were made both static and while spinning at 11 kHz. While spinning at 11 kHz, τ delays were rotosynchronized for the inversion recovery and Hahn echo experiments. A recycle delay exceeding $5*T_1$ was set for every pulse sequence. All experiments were repeated with an empty rotor to verify that the signal detected was solely from the CePO$_4$ sample being studied.

3. Results and discussion

3.1. X-ray diffraction

The XRD results in Fig. 1 show Sample 1 to be phase-pure rhabdophane CePO$_4$. Rhabdophane (PDF 35-0614) is a hydrated, hexagonal form of cerium phosphate, typically expressed as CePO$_4*x$H$_2$O with $x = 0.3-0.5$ [15]. After heating the same powder at 800 °C for 8 h, an irreversible transformation to the monazite phase of CePO$_4$ occurs (Sample 2), as expected based on previous work [13,14]. Monazite (PDF 32-0199) is the monoclinic structure of unhydrated pure CePO$_4$. No residual rhabdophane peaks are observed in this sample, confirming that the transformation to monazite has gone to completion. Monazite CePO$_4$ and residual CeO$_2$ were detected by XRD for both Samples 3 and 4 that were prepared by the aqueous acid synthesis procedure. The amount of residual CeO$_2$ in Sample 3 is lower relative to Sample 4. This is likely due to the significantly lower temperatures used for the synthesis of Sample 4.

3.2. Transmission electron microscopy (TEM)

TEM probed the morphology, composition, and crystallinity of the CePO$_4$ powders. The TEM results in Figs. 2 and 3 show that Sample 1 consists of 10–20 nm by 30–300 nm rod-shaped CePO$_4$ rhabdophane crystals with no detectable amorphous material. Sample 2 consists of 30–80 nm approximately equiaxed monazite crystallites, and also shows no evidence of amorphous phases. The sintered pellet of Sample 3 powder consists of 150–200 nm equiaxed CePO$_4$ grains as well as unreacted 20–60 nm CeO$_2$ particles. In addition, the TEM shows the presence of amorphous intergranular material. The amount of residual CeO$_2$ in Sample 3 is low; the XRD (Fig. 1) indicates approximately 10% of CeO$_2$ by volume and agrees with the
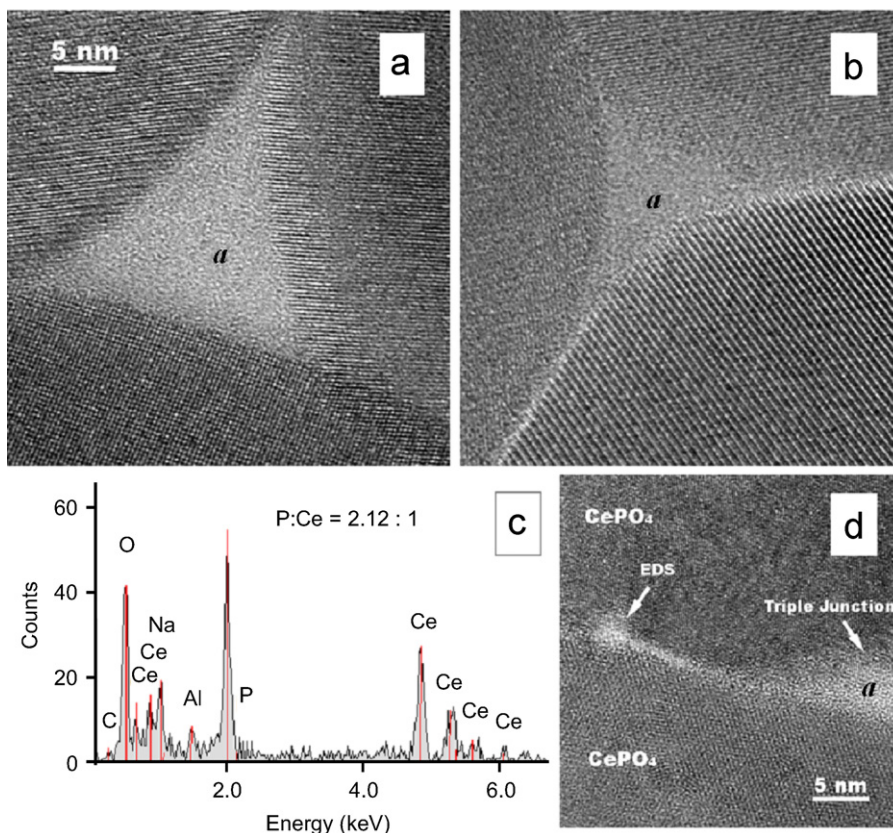
Fig. 4. (a), (b): TEM images of amorphous triple junctions (marked *a*), and grain boundaries in Sample 3 pellet. (c): Typical EDS analysis of grain boundary regions (including triple boundary junctions). The white arrow in (d) indicates where analysis was done. Note the presence of impurities evident in the EDS spectrum, as well as the excess of phosphorus relative to $CePO_4$ in the amorphous regions.

Table 1
Summary of physical properties of samples 1–4 as determined by XRD, TEM, and EDS

Sample	Composition	Crystal structure	Morphology	Particle size	Ce:P ratio
1	Rhabdophane $CePO_4 * xH_2O$	Hexagonal ($P6_222$)	Rod-shaped particles	10-20 nm diameter × 30–300 nm length	53:47
2	Monazite $CePO_4$	Monoclinic ($P2_1/n$)	Spherical particles	30–80 nm diameter	53:47
3	Monazite $CePO_4$/residual CeO_2	Monoclinic ($P2_1/n$)	Spherical particles	100–200 nm $CePO_4$ grains	52:48
				20–60 nm CeO_2 grains	
4	Monazite $CePO_4$/CeO_2 composite	Monoclinic ($P2_1/n$)	$CePO_4$ shell	10–40 nm thick $CePO_4$ shell	Shell-51:49
			CeO_2 core	30–40 nm diameter CeO_2 core	Core-94:6

amount of ceria visible in Fig. 2 (3). Fig. 4 includes an EDS analysis of the intergranular amorphous material in Sample 3. The intergranular material is generally phosphate-rich, and its composition is not uniform throughout the sample. Additionally, sodium and aluminum impurities were detected, presumably introduced from the Pyrex® sample container or the attritor milling process during synthesis. Sample 4 contains 10–40 nm thick polycrystalline $CePO_4$ shells around a core of 30–40 nm diameter CeO_2 particles. It is not clear if this represents an actual reaction morphology, or if it is the result of hetero-agglomeration during TEM specimen preparation. The EDS analysis results show that the $CePO_4$ phase in all of the samples can

be viewed as stoichiometric $CePO_4$ within typical error of EDS (about 2–3%).

The lowest formation temperature of monazite $CePO_4$ reported to date, using a different synthetic route starting with $Ce(CH_3COO)_3 * 2H_2O$ and $(NH_4)H_2PO_4$ in diethylene glycol, was at 180 °C [12]. Crystalline $CePO_4$ in the monazite phase is not typically observed to form from the solution of CeO_2 and H_3PO_4 until a transition temperature of about 660 °C is reached [13], which is much higher than the synthesis temperature of 100 °C for Sample 4. A plausible reason for the formation monazite at this low temperature is that the high surface energy of the CeO_2 nanoparticles promoted their partial dissolution in the

phosphoric acid, forming $CePO_4$ by a solution/precipitation process (Table 1).

3.3. Nuclear magnetic resonance

^{31}P NMR peaks were observed for all four samples (Fig. 5). The shift, relaxation times T_1 and T_2, peak widths, and quantitative population measurements are summarized for all of the observed ^{31}P NMR peaks in Tables 2 and 3. Xu et al. reported they were unable to obtain a ^{31}P NMR signal from non-hydrated monazite $CePO_4$ [5], citing that the paramagnetic interaction between the ^{31}P nucleus and the unpaired electron on Ce^{3+} atoms broadened the peak past their spectral range. We found the static FWHH peak for the monazite $CePO_4$ to be ~500 ppm broad, which is difficult to detect with standard high-resolution NMR methods. In all

data ^{31}P NMR signals quantitatively accounted for all anticipated phosphorus atoms. For example, pure, non-hydrated monazite $CePO_4$ should contain $2.56*10^{21}$ [31]P nuclei/g. Sample 2, confirmed as monazite $CePO_4$ through XRD and TEM, was observed to contain the same number of nuclei/g within experimental uncertainty (Table 2).

To assess further the role of paramagnetism in our NMR data, we conducted variable temperature studies, and found that the ^{31}P NMR peak of monazite $CePO_4$ shifts with temperature (Fig. 6). Such temperature-dependent shifts are consistent with Curie–Weiss paramagnetic behaviour, as seen in [7]Li and [17]O studies of oxides [6,7]. Furthermore, the magnitude of the spin-lattice relaxation times for all ^{31}P lines (Table 2) are also consistent with the presence of paramagnetic ions. The source of the paramagnetism is likely Ce^{3+} ions.

Assignments of the ^{31}P peaks to specific sites within the phosphates proceeds as follows. The peaks at -87 to -94 ppm may be assigned to the P nuclei experiencing paramagnetic (Fermi-contact) shifts in the monazite $CePO_4$ phase, as all samples containing this crystal structure exhibited this signal in their spectra. An estimate of the diamagnetic shift of ^{31}P in monazite can be obtained by taking the infinite temperature limit ($1/T \rightarrow 0$) of the data shown in Fig. 6. The result is a shift of 14 ± 3 ppm for Sample 3. This diamagnetic shift is comparable to the chemical shifts of the Li, Na, and K orthophosphate [8]. Additionally, all samples containing the hydrated rhabdophane phase of $CePO_4$ showed peaks near -55 ppm, which can be assigned to Fermi-contact shifted ^{31}P nuclei in hexagonal phase of cerium phosphate.

The ^{31}P peaks at 9 and 1 ppm appear only in the samples synthesized via aqueous reaction of CeO_2 with phosphoric acid. Given that the intensities of the NMR peaks match well the overall composition of $CePO_4$, we suggest that the peaks at 1 and 9 ppm may be associated with the phosphate-rich amorphous phases observed under TEM. For Sample 3, the
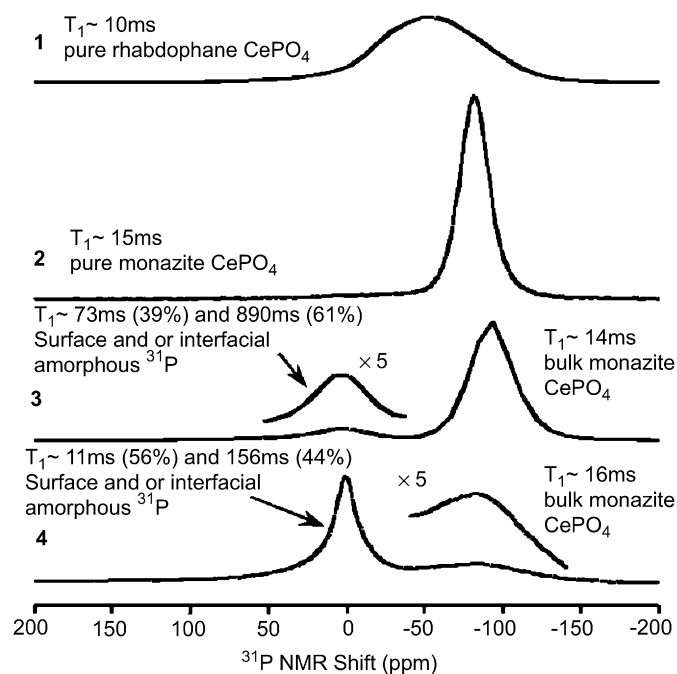

Fig. 5. ^{31}P NMR spectra of the four $CePO_4$ samples obtained in a 1.54 T magnet while spinning the sample at the magic angle at 11 kHz. 0 ppm is referenced to ^{31}P in 85% H_3PO_4. The peak of Sample 3 near 0 ppm and the peak of Sample 4 near -90 ppm were multiplied by 5 relative to the rest of the spectra to make their shapes more apparent. Multiple spin-lattice (T_1) constants were measured for the peaks near 0 ppm, suggesting that the ^{31}P nuclei corresponding to this shift are in multiple chemical environments.

Table 3
Summary of ^{31}P static NMR measurements of the four $CePO_4$ samples

Sample	δ (ppm)	T_1 (ms)	T_2 (ms)	FWHH (ppm)
1	-33	8	0.18	456
2	-72	14	0.19	548
3	-82	14	0.2	510
4	-5	13 (50%), 56 (50%)	0.2	156

Table 2
Summary of ^{31}P 11 kHz MAS NMR measurements of the four $CePO_4$ samples

Sample	δ (ppm)	Peak assignment	T_1 (ms)	T_2 (ms)	FWHH (ppm)	Population ($\times 10^{21}$ nuclei/g)
1	-55	Rhabdophane $CePO_4$ bulk	10	1.7	62	2.6
2	-94	Monazite $CePO_4$ bulk	15	4.1	25	2.5
3	-91	Monazite $CePO_4$ bulk	14	4.2	29	1.9 (89% of total)
3	9	Amorphous intergranular phosphate-rich phase	73 (39%), 890 (61%)	4.0	35	0.2 (11% of total)
4	-87	Monazite $CePO_4$ bulk	16	2.0	70	0.8 (33% of total)
4	1	Amorphous phosphate-rich phase	11 (56%), 156 (44%)	0.5	18	1.6 (67% of total)

intensity ratio of the second peak is approximately 11% of the total ^{31}P signal, which correlates well with the amount of unreacted ceria present (estimated at 10 vol%). As the P:Ce ratio for the synthesis was 1:1, any unreacted oxide results in a corresponding amount of free H_3PO_4. This acid is surmised to form the intergranular phosphate-rich amorphous phase. The intensity ratio of the peak near 0 ppm to the bulk monazite peak at -87 ppm for Sample 4 may be similarly analysed. Approximately 33% of the P intensity is from the peak at -87 ppm, which is associated with the bulk signal from $CePO_4$. The remaining 67% of the population with shift at 9 ppm is inferred to be P nuclei in the amorphous interface or surface regions in Sample 4.

A qualitative understanding of the amorphous phase region may be further developed via analysis of the spin-lattice relaxation times. The short spin-lattice r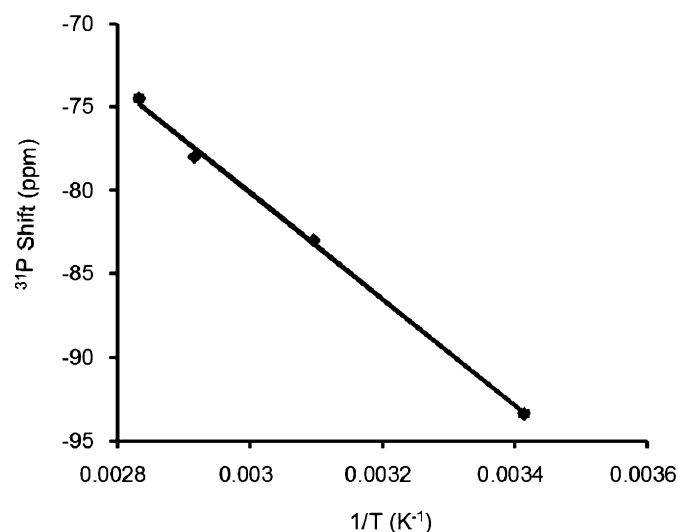elaxation times associated with the peaks emanating from the amorphous phase are suggestive of paramagnetic relaxation, yet the temperature dependence of these shifts (not shown) was found to be very weak. Furthermore, the ^{31}P NMR peaks at 9 and 1 ppm (in Samples 3 and 4, respectively) exhibit bi-exponential spin-lattice relaxation behaviour (Fig. 7), suggesting at least two different relaxation environments for the nuclei corresponding to each peak. Approximately half of the intensity of the NMR peaks attributed to the amorphous phase is characterized by a longer spin-lattice relaxation time (>0.1 s), suggestive of a region containing fewer Ce^{3+} paramagnetic centres. Thus the amorphous phase NMR peaks and relaxation rates are consistent with a core-shell model [9] where a spherical diamagnetic core of material is surrounded by a paramagnetically relaxed shell, with the intensity ratios used for an overall mass balance. Our data can be fit to such a model that yields results consistent with the bulk compostion and length scales observed with electron microscopy; the microscopy data, however, are clearly not consistent with a spherical geometry for the amorphous phase.

4. Conclusion

Powder and sintered samples of nanoparticulate cerium phosphate were prepared through various syntheses. Transmission electron microscopy and X-ray diffraction indicated that in the samples synthesized by reacting ceria with phosphoric acid, an intergranular phosphate-rich amorphous phase persisted even after heat treatments of up to 20 h at 800 °C. The use of ^{31}P-NMR has proved to be a reliable method of distinguishing between phosphorus nuclei in the monazite and rhabdophane phases of $CePO_4$. Additional ^{31}P signals were detected near 0 ppm, their intensity correlating with the amount of unreacted ceria and therefore the amount of phosphate-rich amorhous phases. The complex T1 and T2 relaxation times for these samples supports the presence of the amorphous, phosphate-rich material.
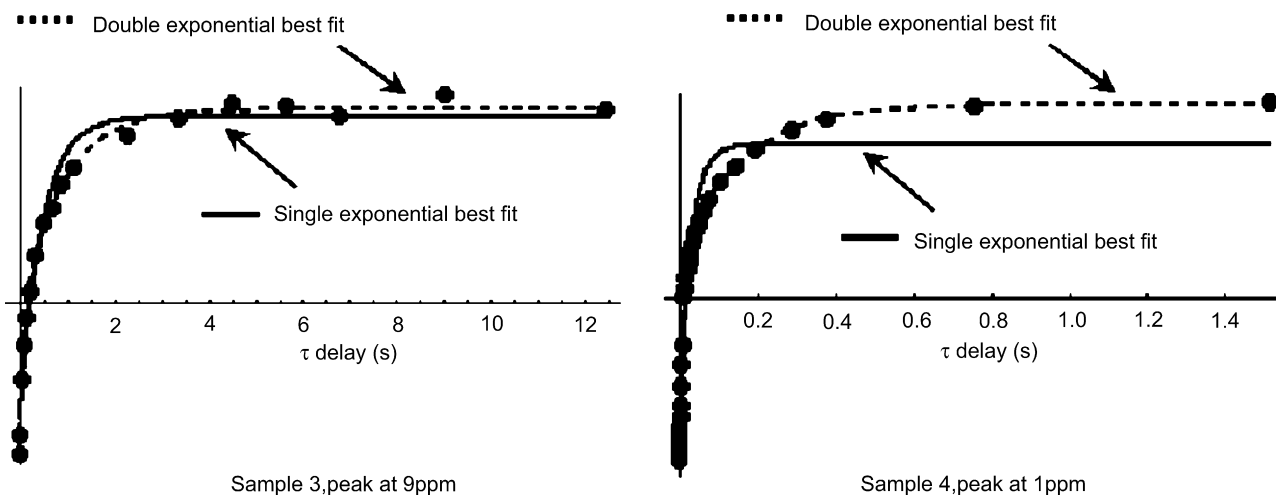

Fig. 6. Variable temperature ^{31}P NMR spectra of the bulk $CePO_4$ peak in Sample 3 obtained in a 1.54 T magnet while spinning the sample at the magic angle at 11 kHz. 0 ppm is referenced to ^{31}P in 85% H_3PO_4.

Fig. 7. Signal intensities of the peaks near 0 ppm in Samples 3 and 4 grow biexponentially with increasing τ delays, corresponding to two separate spin-lattice T_1 constants for each peak.

While the exact nature of the amorphous regions has not been characterized, it is probable that these phosphate-rich intergranular phases will play a role in ionic diffusion and conductivity. Proton conduction in rare-earth phosphates has been attributed to the presence of $(PO_4)H^{-2}$ defects at PO_4 anion sites that are induced by pyrophosphate phases such as P_2O_7 [7,16]. A nano-grained membrane, synthesized as shown above, would result in a higher ratio of intergranular to crystalline $CePO_4$. At the nanoscale, the volume fraction of amorphous interfacial material is no longer negligible, and charge transport through this region may contribute to proton conduction [17]. Exploiting this characteristic of nano-grained $CePO_4$ with phosphorus-rich intergranular phases may well lead to enhanced proton conductivity through the grain boundaries.

Acknowledgments

References

[1] G.W. Beall, L.A. Boatner, J. Inorg. Nucl. Chem. 43 (1980) 101.

[2] Y. Hikichi, T. Nomura, Y. Tanimura, S. Suzuki, J. Am. Ceram. Soc. 73 (12) (1990) 3594.

[3] O.H. Leonardos, Econ. Geol. 69 (1974) 1126–1128.

[4] M. Rappaz, M.M. Abraham, J.O. Ramey, L.A. Boatner, Phys. Rev. B 23 (3) (1981) 1012.

[5] L. Xu, G. Guo, D. Uy, A.E. O'Neill, W.H. Weber, M.J. Rokosz, R.W. McCabe, Appl. Catal. B-Environ. 50 (2004) 113.

[6] B. Gee, C.R. Horne, E.J. Cairns, J.A. Reimer, J. Phys. Chem. B. 102 (1998) 10142.

[7] S.B. Adler, J.A. Reimer, Solid State Ion. 91 (1996) 175.

[8] M. Duncan, Chemical Shift Tensors, second ed., Farragut Press, Madison, WI, 1997.

[9] M. Lopez Granados, F. Cabello Galisteo, P.S. Lambrou, R. Mariscal, J. Sanz, I. Sobrados, J.L.G. Fierro, A.M. Efstathiou, J. Catal. 239 (2006) 410.

[10] N. Kitamura, K. Amezawa, Y. Tomii T. Hanada, N. Yamamoto, T. Omata, Y. Otsuka-Yao-Matsuo, J. Electrochem. Soc. 152 (4) (2004) A658.

[11] H. Onoda, H. Nariai, A. Moriwaki, H. Maki, I. Motooka, J. Mater. Chem. 12 (2002) 1754.

[12] C. Feldmann, H.O. Jungk, J. Mater. Sci. 37 (2002) 3251.

[13] T. Masui, H. Hirai, N. Imanaka, G. Adachi, Phys. Status Solidi A 198 (2) (2003) 364.

[14] S. Lucas, E. Champion, D. Bernache-Assollant, G.J. Leroy, J. Solid State Chem. 177 (2004) 1312.

[15] S. Lucas, E. Champion, D. Bregiroux, D. Bernache-Assollant, F. Audubert, J. Solid State Chem. 177 (2004) 1302.

[16] K. Amezawa, H. Maekawa, Y. Tomii, N. Yamamato, Solid State Ion. 145 (2001) 233–240.

[17] P. Heitjans, S. Indris, J. Phys: Condens. Matter 15 (2003) R1257.